Temporal and spectral study of the X-ray pulsar 2S 1553–542 during the 2021 outburst

MANOJ MANDAL and SABYASACHI PAL*

Midnapore City College, Kuturia, Bhadutala 721129, India.
*Corresponding author. E-mail: sabya.pal@gmail.com

Abstract. We study the timing and spectral properties of the X-ray pulsar 2S 1553–542 using the NuSTAR and NICER during the outburst in January–February 2021. During the outburst, the spin period of the neutron star was $P \sim 9.2822$ s based on NuSTAR data. The pulse profiles are studied using different NICER observations, which implies that the profile is more or less sinusoidal with a single peak and the beaming patterns are dominated mainly by the pencil beam. The NICER spectra of the source are studied for different days of the outburst. They can be well described by a model consisting of a blackbody emission, power law and photoelectric absorption component. The variation of spectral parameters with luminosity is studied over the outburst. The photon index shows anti-correlation with luminosity below the critical luminosity, which implies that the source was accreting in the sub-critical accretion regime during the NICER observations. We also report the anti-correlation between pulsed fraction (PF) and luminosity of the 2S 1553–542 using NICER observations. The evolution of spin-up rate with luminosity is studied during the outburst, which implies that both are strongly correlated. The torque-luminosity model is applied to estimate the magnetic field at different spin-up rates. The magnetic field is estimated to be $\simeq 2.56 \times 10^{12}$ G from the torque-luminosity model using the source distance of 20 kpc. The magnetic field is also estimated using the critical luminosity, consistent with our findings.

Keyword. Accretion, accretion discs—stars: magnetic field—stars: neutron-pulsars: individual: 2S 1553–542.

1. Introduction

During the Galactic plane survey, the X-ray transient 2S 1553–542 was discovered using Small Astronomy Satellite 3 (SAS-3) in 1975 ([Apparao *et al.* 1978](#)). A strong pulsation with the period of 9.3 was found ([Kelley *et al.* 1983](#)) with an orbital period P_{orb} of nearly 30 d. During the outburst in 2007–2008, the spectral and timing properties of the X-ray pulsar were studied using the Rossi X-ray Timing Explorer (RXTE) ([Pahari & Pal 2012](#)). The RXTE allowed us to improve the orbital parameters of the system and to trace the spectral evolution in the energy range of 2.5–30 keV. During the outburst, the spin period P_{spin} was 9.2829 ± 0.0003 s with period derivative $\dot{P} \sim 10^{-9}$ s s^{-1} and the pulsed fraction showed a negative correlation with the time of the outburst. The pulse profile was single-peaked and featureless, and variability in

the pulse profile was observed during the outburst. An energy-dependent pulse profile was also studied, but no significant variation was found in the pulse profile with energy. Significant variability of the pulse fraction was observed in RXTE/PCA observations and PF was decreased with the decay of the flaring activity. The power density spectrum showed an interesting feature. The fundamental line with its five harmonics was visible. The variation of different spectral parameters with different orbital phases was studied, and it was shown that the source hard X-ray spectra in all available intensity states could be well explained with the combination of a broken power law and a blackbody component (with temperature varying between 2.5 and 4 keV) ([Pahari & Pal 2012](#)).

The X-ray pulsar 2S 15553–542 went through another outburst in 2015. During this outburst, the temporal and spectral properties of the source were studied using

Chandra and NuSTAR data (Tsygankov *et al.* 2016). Based on the Fermi/GBM data, the orbital parameters of the system were substantially improved, which allowed determining the spin period of the neutron star $P = 9.27880(3)$ s and a local spin-up $\dot{P} = -7.5 \times 10^{-10}$ s s^{-1} due to the mass accretion during the NuSTAR observations. Assuming accretion from the disc and using standard torque models, the distance to the system was estimated as $d = 20 \pm 4$ kpc. From the timing analysis, the single-peak-shaped pulse profile was found with a barely noticeable dependence on energy, which is quite similar to the previous results (Pahari & Pal 2012). The cyclotron absorption feature near 23.5 keV was found during the declining stage of the outburst with a corresponding magnetic field strength $\sim 3 \times 10^{12}$ G (Tsygankov *et al.* 2016). During the 2021 outburst, the energy spectrum was studied using NuSTAR, and the luminosity dependence of the cyclotron line was investigated (Malacaria *et al.* 2022). A state transition is reported above the critical luminosity of 4×10^{37} erg s^{-1} (Malacaria *et al.* 2022).

The X-ray pulsar went through an outburst after a quiescence of nearly six years as detected by Burst Alert Telescope (BAT) onboard Swift and Gas Slit Camera (GSC) onboard MAXI on January 2021 (Mandal *et al.* 2021). The X-ray flux started to increase in early January of 2021, and the duration of the outburst was nearly six weeks. We study different temporal and spectral properties of the X-ray pulsar in the soft X-ray band using the Neutron star Interior Composition Explorer (NICER) and in the hard X-ray band using the Nuclear Spectroscopic Telescope Array (NuSTAR). We also look for the evolution of the timing and spectral properties in broadband during the outburst in 2021 using NICER and NuSTAR data. The emission mechanism, beaming patterns, and accretion regime are investigated using timing and spectral study during the outburst.

We have studied the variation of photon index and pulse fraction with luminosity during the outburst. We also look at the evolution of the pulse profile, spin-up rates and beaming patterns of the source at different luminosities. We look for any correlation between the spin-up rates and luminosity for the source during the outburst. The torque-luminosity model is used to estimate the magnetic dipole moment and magnetic field from the spin-up rates and luminosity correlation.

The data reduction and analysis methods are discussed in Section 2. We have summarized the results of the current study in Section 3. The discussion and conclusion are summarized in Sections 4 and 5, respectively.

2. Observation and data analysis

An outburst from the X-ray pulsar 2S 1553–542 was detected in 2021 and followed up using different satellites in multi-wavelength regions. The Burst Alert Telescope (BAT) onboard The Neil Gehrels Swift Observatory (Gehrels *et al.* 2004) is sensitive to hard X-ray (15–50 keV) (Krimm *et al.* 2013). To study the evolution of the outburst, we utilize data from various all-sky X-ray monitors, including Swift/BAT (15–50 keV), MAXI/GSC (2–20 keV), Fermi/GBM (12–25 keV). NuSTAR data was taken at the peak of the 2021 outburst and NICER data were taken on various days of the outburst. We used HEASOFT version 6.28 for the data reduction and analysis.

We have used the results of the BAT transient monitor during the outburst provided by the BAT team. The flux peaked in the third week of January and continued for around six weeks as seen by the Swift/BAT. In the present study, we used the measurements of spin frequency and 12–25 keV pulsed flux measurements with the Fermi/GBM (Camero-Arranz *et al.* 2009; Finger *et al.* 2009). The Fermi/GBM also detected the outburst from 2S 1553–542, which continued for almost six weeks with a peak pulsed flux of ~ 0.24 keV cm^{-2} s^{-1} on MJD 59240.

2.1 *NuSTAR observation*

The NuSTAR observatory comes with two co-aligned, identical X-ray telescope systems operating in a wide energy range of 3–79 keV. Separate solid-state CdZnTe pixel detector systems in each telescope, usually referred to as focal plane modules A and B (FPMA and FPMB; Harrison *et al.* 2013), have a spectral resolution of 400 eV at 10 keV and 900 eV at 68 keV (FWHM), respectively. NuSTAR performed an observation of 2S 15553–542 close to the peak of the outburst (MJD 59236.95) with a total exposure of 28.35 ks. The observation log of NuSTAR is shown in Table 1. The data is reduced using the NuSTARDAS pipeline provided under HEASOFT with the latest caldb and we defined the source and background using ds9. The light curve and spectra of the source and background are generated from circular regions centering the source with radii of 50 arcsec and 100 arcsec using nuproducts scripts provided by the NuSTARDAS pipeline. The light curve has been extracted using the science event data in different energy ranges with bin sizes of 0.1 s for both the modules (FPMA/FPMB) of NuSTAR. The efsearch task in FTOOLS is used to find the best

**Table 1.** Log of NuSTAR and NICER observations

Instrument	Start time (MJD)	Date (yyyy-mm-dd)	Exposure (ks)	Obs. ID
NuSTAR	59236.95	2021-01-22	28.3	90701302002
NICER	59268.08	2021-02-23	1.4	3202030101 (Obs 1)
	59271.62	2021-02-26	2.0	3202030102 (Obs 2)
	59272.02	2021-02-27	0.4	3202030103 (Obs 3)
	59274.02	2021-03-01	0.3	3202030104 (Obs 4)

period in the time series of the barycenter and background corrected data sets. The folding method of the light curve over a trial period is used to get the best period by χ^2 maximizing process (Leahy 1987) over 32 phase bins in each period. After getting the best spin period, pulse profiles are obtained using the `efold` task in `FTOOLS` by folding light curves with the best spin period.

2.2 *NICER observation*

The NICER onboard the International Space Station is a non-imaging, soft X-ray telescope. The main part of NICER is the X-ray Timing Instrument (XTI), which operates in a soft X-ray region (0.2–12 keV) (Gendreau *et al.* 2016). NICER observed the source for one week during the declining phase of the outburst. Table 1 summarizes the log of NICER observations used for the current study. The NICER data has been processed with `NICERDAS` in `HEASOFT`. We have created clean event files by applying the standard calibration and filtering tool `nicerl2` to the unfiltered data. We have extracted light curves for different energy ranges with a bin size of 0.1 s and spectra using `XSELECT`. The task `barycorr` is used to apply barycentric corrections for timing analysis.

We have fitted the NICER spectra in `XSPEC` with the redistribution matrix file (RMF) and NICER ancillary response file (ARF) provided by NICER team.[1] We also extracted NICER spectra for different days of the outburst during the declining phase. The good time intervals are selected for the timing analysis according to the following criteria: The ISS was not in the South Atlantic Anomaly (SAA) zone, the source elevation was >20° above the Earth limb, and the source direction was at least 30° from the bright Earth. The
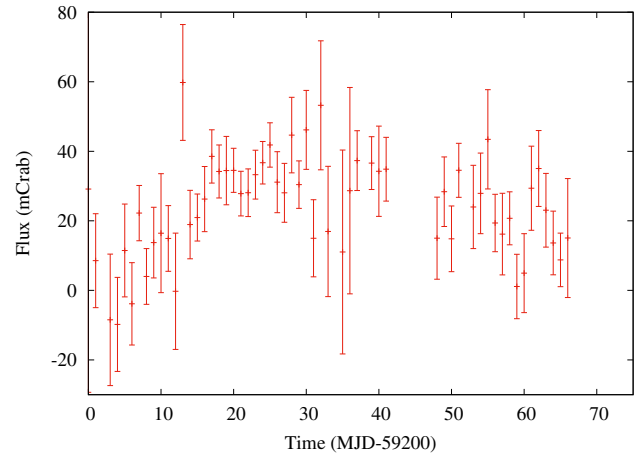
Figure 1. Swift/BAT (15–50 keV) detects an outburst form 2S 1553–542 during January–February 2021.

background corresponding to each epoch of the observation was simulated by using the `nibackgen3C50`[2] tool (Remillard *et al.* 2022).
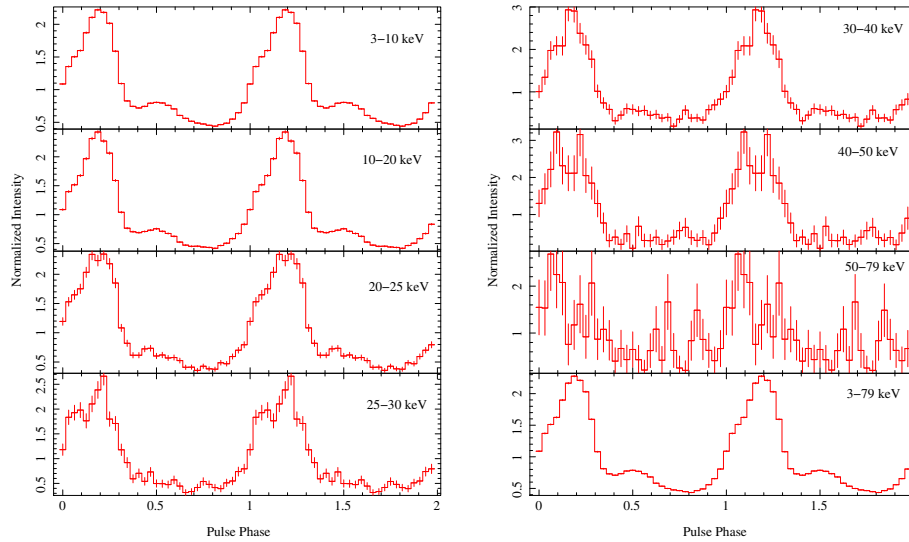
3. Results

The X-ray pulsar 2S 15553–542 went through an outburst during January–February 2021, detected by Fermi/GBM, Swift/BAT[3] and MAXI/GSC which reached a maximum flux during the last week of January 2021. We used MAXI (Matsuoka *et al.* 2009) final data products (light curves) as well as the Fermi (Finger *et al.* 2009; Meegan *et al.* 2009) pulse frequencies and pulsed flux evolution data. Figure 1 shows the variation of flux during the outburst using Swift/BAT (15–50 keV). The total duration of the outburst was around six weeks, which started in the first week of January 2021 and continued till the second week of February 2021.

Figure 2. Energy dependent pulse profiles of 2S 15553–542 using data from NuSTAR observation during the 2021 outburst.

We have summarized the results of the timing and spectral analysis of 2S 15553–542 during the recent outburst in 2021 using data from NuSTAR and NICER.

3.1 *Evolution of timing parameters*

We have investigated the evolution of the different timing parameters during the outburst using NuSTAR, and NICER observations. The spin period of the pulsar during the outburst was $P = 9.2822 \pm 0.0001$ s using NuSTAR data, which is consistent with the pulse period evolution history as recorded with Fermi/GBM during the outburst.[4]

We also look at the energy dependence of pulse profiles as well as the temporal variation of pulse profiles during the outburst. Figure 2 shows the energy-dependent pulse profiles for different energy ranges of NuSTAR observation. The variation of the pulse profile over different energy bands is shown in Figure 2. The pulse profile shows a single-peaked, nearly sinusoidal nature. The pulse profile shows an evolution near the fundamental cyclotron line energy ∼27 keV (Malacaria *et al.* 2022) as the scattering cross-section changes near CRSF, the emission mechanism, and the beaming pattern are affected. Figure 2 also shows that in the energy ranges of 25–30 keV, the pulse profile changes, which corresponds to the CRSF line energy.

Pulse Fraction (PF) variation with energy is studied during the NuSTAR observation. PF can be defined as the ratio between the difference of maximum intensity (I_{max}) and minimum intensity (I_{min}) to their sum:

$[(I_{max} - I_{min})/(I_{max} + I_{min})]$. We have also calculated the RMS pulse fraction using the following formula:

$$\mathrm{PF} = \frac{1}{\sqrt{N}} \left[\sum_{i=1}^{N} (p_i - \bar{p})^2 \right]^{\frac{1}{2}}, \qquad (1)$$

where N is the total number of phase bins, p_i is the count rate in the ith phase bin of the pulse profile and $\bar{p}$ is the average count rate. Figure 3 shows the variation of PF for different energy ranges for which the energy-resolved pulse profile is studied. The horizontal bars represent the energy ranges for which the PF is calculated. The PF shows a positive correlation with energy. We have found that the RMS pulse fraction increases from ∼55% (3–10 keV) to ∼90% (40–50 keV) during the NuSTAR observation.

Figure 3 shows the variation of pulse fraction with energy using NuSTAR data. Figure 3 shows local maxima near ∼27 keV, which is close to the CRSF fundamental line. The scattering cross-section changes near the CRSF, which affects the beaming pattern and pulse profile. We have found a local feature in the pulsed fraction near the cyclotron line at 27 keV and the pulse profile (25–30 keV) also showed an evolution near this energy. The beaming pattern may be affected near the cyclotron line energy, which impacts on timing parameters.

Figure 4 shows the evolution of the spin period and pulsed flux (12–25 keV) during the outburst using Fermi/GBM and the corresponding spin periods provided by Fermi/GBM are shown in the upper panel of the figure. The pulsed flux reached a maximum value of ∼0.24 keV cm^{-2} s^{-1}. The top panel of this figure
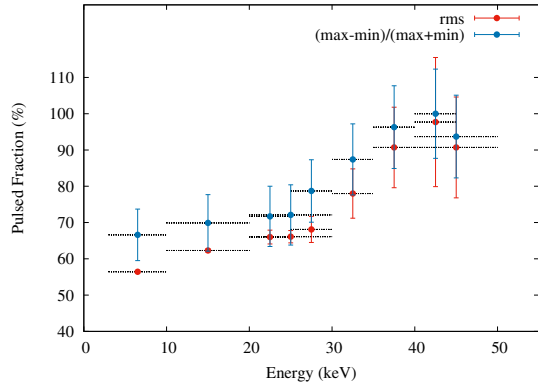
Figure 3. Evolution of pulse fraction with energy using NuSTAR observation. The horizontal error bars indicate the energy range for which PF is estimated and the vertical error bars indicate the errors of corresponding measurements, respectively. The figure shows local maxima near cyclotron line energy ∼27 keV.

implies that the pulse period of the X-ray pulsar continuously decreased during the outburst.

The evolution of pulse profiles is studied using different NICER observations at different luminosity levels during the outburst. Figure 8 shows pulse profiles for different NICER observations. The pulse profiles do not show significant evolution during different NICER observations. The NICER profiles are more or less single peaks and nearly sinusoidal during observations.

We look for any correlation between the spin-up rate and luminosity for the source. We have used the values of spin-frequencies during the outburst, which are provided by the Fermi/GBM team. We utilized 18 spin frequency (ν) measurements made during our study. The spin frequency measurements were taken at equal intervals of about four days. Each of the three subsequent frequency measurements with time was fitted using a linear function. The spin-up rate ($\dot{\nu}$) was determined from the slope of the linear function during a 12-day interval using the χ^2 minimization method. The method was then repeated for the following three frequency measurements, and so on, Kabiraj & Paul (2020). As a result, from 18 spin frequencies, we obtained six spin-up rates. We have also included 21 frequency measurements from the 2015 outburst to obtain good fitting results, which provided additional seven spin-up rates.

We have used the NuSTAR data to estimate unabsorbed flux (3–79 keV) during the NuSTAR observation of the 2021 outburst. We calculate the conversion factor by which the GBM pulsed flux is related to the total flux from the NuSTAR observation. We multiplied all GBM fluxes with the estimated conversion factor to convert them into the total flux. We have used the average value
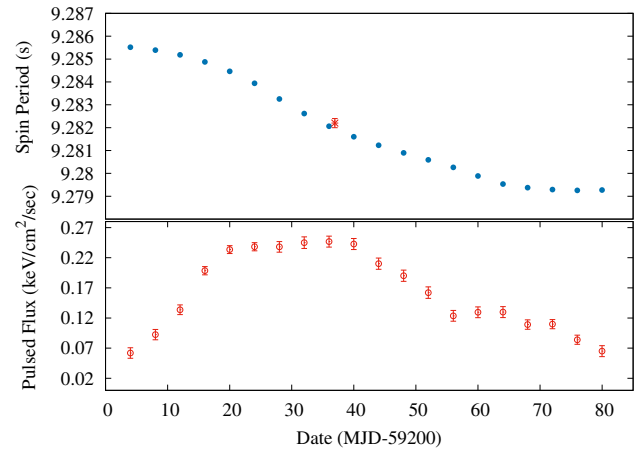
Figure 4. The variation of the spin period during the outburst using Fermi/GBM is shown with blue circles. The red asterisks show the pulse period calculated from NuSTAR observation. The bottom panel shows the evolution of pulsed flux (12–25 keV) using Fermi/GBM. The vertical bars represent errors in corresponding measurements.

of total flux for three consecutive points over the same intervals, which are used to determine $\dot{\nu}$. Finally, the X-ray flux estimates the luminosity for a source distance of ∼20 kpc (Tsygankov *et al.* 2016). The X-ray luminosity of the source is estimated from the Fermi/GBM pulsed flux provided by GBM team by multiplying a flux conversion factor of 6.85×10^{-9} erg keV^{-1}.

The variation of spin-up rate with luminosity is shown in Figure 7. The variation of spin-up rate with luminosity is fitted using a power law, which indicates the spin-up rate and luminosity are positively correlated. The spin frequency derivatives vary between ∼(0.4–2.0) $\times 10^{-11}$ Hz s^{-1}, which is estimated from spin frequency evolution history as provided by Fermi/GBM. The luminosity is varied between ∼(3–8) $\times 10^{37}$ erg s^{-1}, which is estimated from the Fermi/GBM pulsed flux using a multiplying factor.

3.2 *Phase average energy spectra*

We have studied the energy spectra for different outburst days using NICER observations and looked for the variation of different spectral parameters. The energy spectra with the best-fitted model are shown in Figure 5, where the bottom panels of Figure 5 show the residuals. We have extracted the energy spectrum for different observations from NICER and fitted them in XSPEC, independently varying the model parameters for different models. The energy spectrum of the X-ray pulsar can be well fitted with a power-law (power law in XSPEC) and a blackbody emission component (bbody in XSPEC) along with photoelectric absorption (phabs

in XSPEC). The spectra in the energy range of 0.6–10 keV is well described by blackbody emission with temperature (kT_{bb}) $\sim$ 0.9–1.3 keV and a neutral absorption of an equivalent hydrogen column density $\sim 3.5 \times 10^{22}$ cm^{-2}. Table 2 shows the evolution of different spectral parameters with the best-fitted values for different outburst days. The photon index varied between $\sim$(0.2 and 1.1) during different NICER observations. For the NICER observations 3 and 4, the spectra are fitted well with a power law component along with a photoelectric absorption. The additional black body component is unnecessary to fit these two NICER spectra.

3.3 *Luminosity dependence of pulsed fraction and photon index*

We have looked for the variation of photon index and pulsed fraction with luminosity during the outburst.
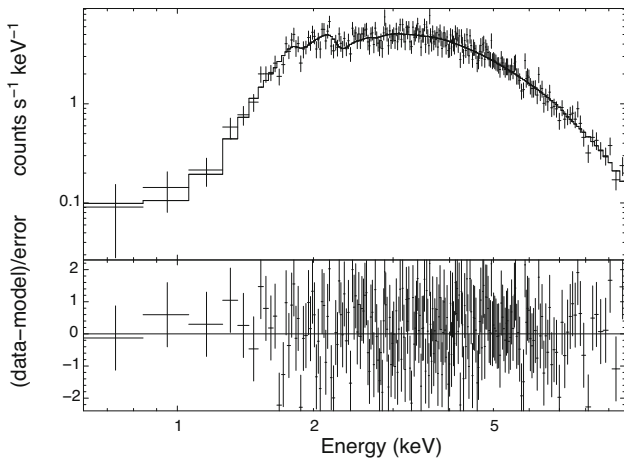
Figure 5. NICER energy spectrum for Obs 3, fitted with phabs×(power law). Residuals are shown in the bottom panels of the figure.

The top panel of Figure 6 shows the variation of the photon index with luminosity. The photon index is estimated from the power-law continuum of energy spectra. The top panel of Figure 6 shows a weak anti-correlation between the photon index and luminosity. The bottom panel of Figure 6 shows the evolution of PF with luminosity using NICER observations. A negative correlation between luminosity and pulse fraction is observed during NICER observations below the luminosity of 1.8×10^{37} erg s^{-1}. The pulsed fraction varies between 40% and 48% as estimated using NICER observations. The luminosity varies between (1.25–1.70) $\times 10^{37}$ erg s^{-1} during the NICER observation. The luminosity is estimated for a source distance of 20 kpc from NICER flux in the energy range of 0.6–10 keV.

4. Discussion

We present the results from timing and spectral analysis of 2S 1553–542 during the recent outburst in January–February 2021 using the NuSTAR and NICER data. The critical luminosity for 2S 1553–542 is estimated to be $\simeq 3.7 \times 10^{37}$ erg s^{-1} by Becker *et al.* (2012). The energy dependence of the pulse profile is studied to investigate the evolution of the individual peaks and beaming pattern of the pulse profile of the pulsar with different energies. The pulse profile shows a single peak and a nearly sinusoidal nature. In the energy range of 25–30 keV, the pulse profile shows an additional feature that is close to the line energy. The pulse fraction shows a trend to increase with energy, which is typical for an X-ray pulsar (viz., Lutovinov & Tsygankov 2009). The pulse fraction shows a local feature near the cyclotron line energy during the NuSTAR observation. We study the temporal variability of the pulse profile and pulse

Table 2. Spectral fitting parameters for best-fitted models for different NICER observations

| Model | Parameters | NICER | | | |
		Obs 1	Obs 2	Obs 3	Obs 4
	N_H	3.0 ± 0.3	3.2 ± 0.3	3.8 ± 0.2	3.5 ± 0.2
phabs × (po + bb)	Γ	$0.62^{+0.3}_{-0.4}$	$0.67^{+0.24}_{-0.29}$	1.08 ± 0.08	1.0 ± 0.1
	kT_{bb} (keV)	$1.2^{+0.3}_{-0.12}$	$1.0^{+0.12}_{-0.14}$	–	–
	norm$_{bb}$, 10^{-3}	1.23 ± 0.6	0.6 ± 0.4	–	–
	Reduced χ^2 (d.o.f)	1.13 (606)	1.07 (626)	1.02 (220)	0.99 (174)
	Total flux (0.6–10 keV)	3.55	3.04	2.87	2.63

N_H: hydrogen column density (10^{22}, cm^{-2}), Γ: power-law photon index, kT_{bb}: blackbody temperature, flux: (10^{-10}, erg cm^{-2} s^{-1}). All reported errors are at 1σ c.l., obtained from err tool from XSPEC.
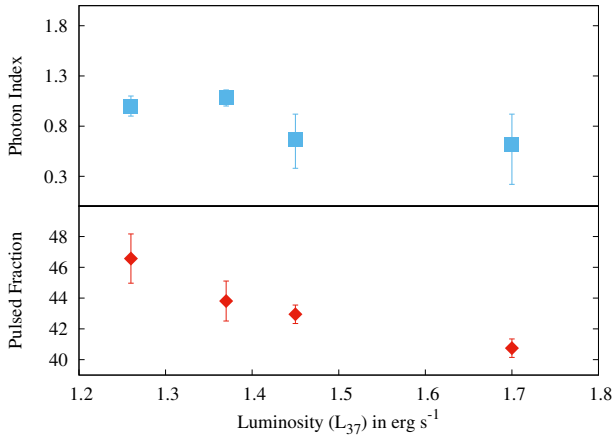
Figure 6. Evolution of photon index and pulsed fraction with luminosity. Luminosity is estimated from the NICER X-ray flux in the energy range of 0.6–10 keV for a source distance of 20 kpc.

fraction during the outburst using NuSTAR and NICER observations during the outburst. Earlier, the pulse fraction varied with time during the outburst and decreased gradually with the outburst, as observed by Pahari & Pal (2012).

The beaming pattern of a pulsar is affected by its luminosity. When the source luminosity goes below the critical luminosity (subcritical regime), accreting material falls directly on the surface of the neutron star, producing a 'pencil beam' X-ray emission. Emission escapes from the top of the column for the pencil beam pattern (Burnard *et al.* 1991). However, the beaming patterns can be more complex than a pencil or fan beam (Kraus *et al.* 1995; Becker *et al.* 2012). The pulse profile of the pulsar 2S 1553–542 during the 2021 outburst is a nearly single peak feature. These patterns are governed mainly by the 'pencil beam' form.

Critical luminosity (L_{crit}) is important to define two accretion regimes of a source. In the subcritical regime, the source luminosity is lower than the critical luminosity, and at the critical luminosity, a state transition occurs from the subcritical to the supercritical regime. The radiation pressure in the supercritical regime is high enough to stop accreting matter at a distance above the neutron star, generating a radiation-dominated shock (Basko & Sunyaev 1976; Becker *et al.* 2012). In the subcritical regime, accreted material reaches the surface of a neutron star through nuclear collisions with atmospheric protons or Coulomb collisions with thermal electrons (Harding 1994). Changes in cyclotron line energy, pulse profiles and spectral shape can be used to probe these accretion regimes (Parmar *et al.* 1989; Reig & Nespoli 2013).

Near the cyclotron line energy, a distinct change in pulse profile and pulsed fraction was reported for a few sources, such as 1A 1118–61, Her X-1, GX 301–2, and 1A 0535+262 (Mandal & Pal 2022). Earlier, Lutovinov & Tsygankov (2009) summarized different sources for which a distinct change in pulse profile and pulse fraction was observed. A non-uniform increase in pulsed fraction with energy was observed for different sources like V 0332+53, Vela X-1, Her X-1, GX 1+4, 1A 0535+262, and 4U 0115+63 and a local maxima near cyclotron line energy and harmonics was found (Lutovinov & Tsygankov 2009).

The pulsed fraction exhibits a transition above the critical luminosity for a few sources. In the supercritical accretion regime, the pulsed fraction negatively correlates with luminosity. During the 2020 giant outburst, 1A 0535+262 showed a positive correlation between the PF and luminosity in low luminosity and above the critical luminosity. The correlation was reversed to a negative correlation (Mandal & Pal 2022). We report an anti-correlation between the PF and luminosity for 2S 15553–542 during the 2021 outburst. Above the critical luminosity, the impact from the unpulsed photons leaving through the side walls of the column increases, which may affect the beaming patterns of the pulsar.

The 0.6–10 keV NICER spectra are fitted with a power-law and blackbody along with a photoelectric absorption model. Earlier, the X-ray spectrum of the source using XRT (0.5–10 keV) was modeled with simple model components like power-law or a blackbody emission along with photoelectric absorption (Lutovinov *et al.* 2016). Earlier, an iron emission line near 6.4 keV was reported from RXTE and NuSTAR observations (Pahari & Pal 2012; Tsygankov *et al.* 2016). We have added a Gaussian component to the model to check the significance of the iron emission line, and it did not improve the goodness of the fit of NICER spectra. The evolution of different spectral parameters is studied during the outburst, which suggests that the spectra from different NICER observations can be explained with a simple model like power-law and blackbody along with photoelectric absorption.

A negative correlation between the photon index and NICER flux is observed. The photon index decreases with an increase in X-ray flux, which indicates a 'harder when brighter' trend. In the subcritical accretion regime, the negative correlation implies the hardening of the power-law continuum with flux. Several sources showed a significant variation in the $L - \Gamma$ diagram close to critical luminosity. The transition from a negative to positive correlation was seen in the $L - \Gamma$ diagram as luminosity increased (Reig & Nespoli 2013).
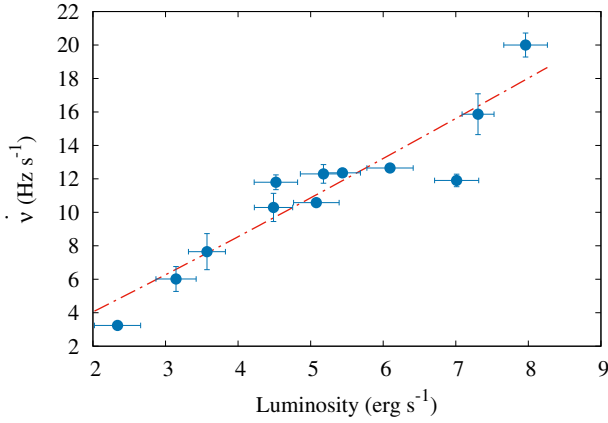
Figure 7. Variation of spin change rate (in unit of 10^{-12} Hz s^{-1}) with luminosity (in unit of 10^{37} erg s^{-1}). The dotted blue line represents the best power-law fit of data points that gives a power-law index of 1.08 ± 0.17.

Earlier, in the subcritical regime, a negative correlation was reported for the sources like 1A 1118–612, GRO J1008–57, XTE J0658–073, and a transition in the correlation of $L - \Gamma$ was observed for the sources 1A 0535+262 (Mandal & Pal 2022), 4U 0115+63, EXO 2030+375 (Epili *et al.* 2017; Jaisawal *et al.* 2021), 2S 1417–624 (Serim *et al.* 2022) and KS 1947+300 (Reig & Nespoli 2013).

Figure 7 shows that the X-ray pulsar 2S 1553–542 pulse frequency derivatives correlate with luminosity. A correlation between spin-up rate and X-ray flux was seen during outbursts for several transient systems. This correlation was explained in terms of accretion. For example, GRO J1744–28 (Bildsten *et al.* 1997), 2S 1417–624 (Finger *et al.* 1996a; Mandal & Pal 2022b), A 0535+26 (Finger *et al.* 1996b; Bildsten *et al.* 1997), EXO 2030+375 (Parmar *et al.* 1989; Reynolds *et al.* 1996) and SAX J2103.5+4545 (Baykal *et al.* 2002) showed correlation between spin-up rate and X-ray flux.

We have tried to calculating the magnetic dipole moment and the surface magnetic field of 2S 1553–542 using the accreting torque model and the observed spin-up rate. Transient X-ray pulsars are known to have a correlation between the spin-up rate and luminosity as (Ghosh & Lamb 1979b; Sugizaki *et al.* 2017):

$$\dot{\nu}_{12} = 2.0 n \zeta^{\frac{1}{2}} \mu_{30}^{\frac{2}{7}} R_6^{\frac{6}{7}} M_{1.4}^{-\frac{3}{7}} I_{45}^{-1} L_{37}^{\frac{6}{7}}, \qquad (2)$$

where μ_{30}, $\dot{\nu}_{12}$, R_6, $M_{1.4}$ and I_{45} are the magnetic dipole moment, spin frequency derivative, radius, mass and the moment of inertia of the neutron star given in the units of 10^{-12} Hz s^{-1}, 10^{30} G cm^3, 10^6 cm, 1.4 $M_\odot$

and 10^{45} g cm^2, respectively. L is the X-ray luminosity in the unit of 10^{37} erg s^{-1}. According to the Ghosh & Lamb (1979a, b) model, under slow-rotator condition, $n \sim 1.39$ and $\zeta \sim 0.52$. Therefore, Equation (1) reduces to Sugizaki *et al.* (2017):

$$\dot{\nu}_{12} = kL_{37}^{\alpha}, \qquad (3)$$

where $k = 2.0 \mu_{30}^{\frac{2}{7}}$ and $\alpha = \frac{6}{7}$. For the nominal values of $I_{45} = R_6 = M_{1.4} = 1$, measurements of the $\dot{\nu}$ vs. L give a rough estimation of the magnetic dipole moment of the pulsar. From the L vs. $\dot{\nu}$ plot, we have calculated k and α as 1.92 ± 0.58 and 1.08 ± 0.17, respectively, using the best-fit results. The estimated α value is close to the theoretical value. Figure 7 shows the correlation between the spin-up rate and luminosity and the dotted line represents the best-fitted result. From the best-fit result, we may write Equation (2) as:

$$\dot{\nu}_{12} = (1.92 \pm 0.58) L_{37}^{1.08 \pm 0.17}. \qquad (4)$$

The magnetic dipole moment of the pulsar can be written in the form:

$$2.0 \mu_{30}^{\frac{2}{7}} = 1.92 \pm 0.58; \quad \mu_{30} \simeq 0.87 \pm 0.01. \qquad (5)$$

The surface magnetic field can be calculated from the magnetic moment (μ_{30}) and radius (R_6) of the pulsar as:

$$\mu_{30} = \frac{1}{2} B_{12} R_6^3 \phi(x), \qquad (6)$$

$\phi(x)$ is the correlation factor, for typical NS, $\phi(x) \sim 0.68$. The magnetic field can be written as:

$$B_{12} = 2 \times \frac{\mu_{30}}{0.68} \qquad (7)$$

for $\mu_{30} \simeq 0.87$, the magnetic field is estimated to be $\simeq (2.56 \pm 0.03) \times 10^{12}$ G.

We have also estimated the magnetic field corresponding to the critical luminosity. Earlier, the critical luminosity was reported to be 4×10^{37} erg s^{-1} (Malacaria *et al.* 2022). For a typical neutron star, the magnetic field is related to the critical luminosity as Becker *et al.* (2012),

$$L_{\text{critical}} = 1.5 \times 10^{37} \left(\frac{B}{10^{12} \, \text{G}} \right)^{\frac{16}{15}} \text{erg s}^{-1}. \qquad (8)$$

The magnetic field corresponding to the critical luminosity 4×10^{37} erg s^{-1} is estimated to be 2.5×10^{12} G for a source distance of 20 kpc. This value of the estimated magnetic field closely matches our results.

5. Conclusion

We summarized the results of the timing and spectral analysis of the poorly studied X-ray pulsar during the outburst in 2021. The spin period of the neutron star was found to be $P \sim 9.2822$ s based on NuSTAR data. The pulse profile using NuSTAR shows a single peak feature, and near the cyclotron line energy, an additional feature in the pulse profile is observed. The beaming patterns were mostly dominated by pencil beams during the NICER and NuSTAR observations. The pulse fraction positively correlates with energy with a local feature near the cyclotron line energy. The pulse fraction shows a negative correlation with luminosity ($Lx < 1.8 \times 10^{37}$ erg s^{-1}) for NICER observations. The source enters the supercritical regime at the highest flux above the critical luminosity. The spectrum can be described using an absorbed power law with a blackbody component. A variation of the photon index with luminosity is studied, which implies that the photon index decreases with an increase in luminosity during NICER observations. The negative correlation implies that the source was in the sub-critical accretion regime during those observations. The variation of spin-up rate with luminosity is studied for 2S 1553–542 during the outburst, which suggests the spin-up rate is strongly correlated with luminosity. The magnetic field is estimated using the torque-luminosity model with different spin-up rates. The magnetic field is calculated to be 2.56×10^{12} G from the torque-luminosity model for a source distance of 20 kpc.
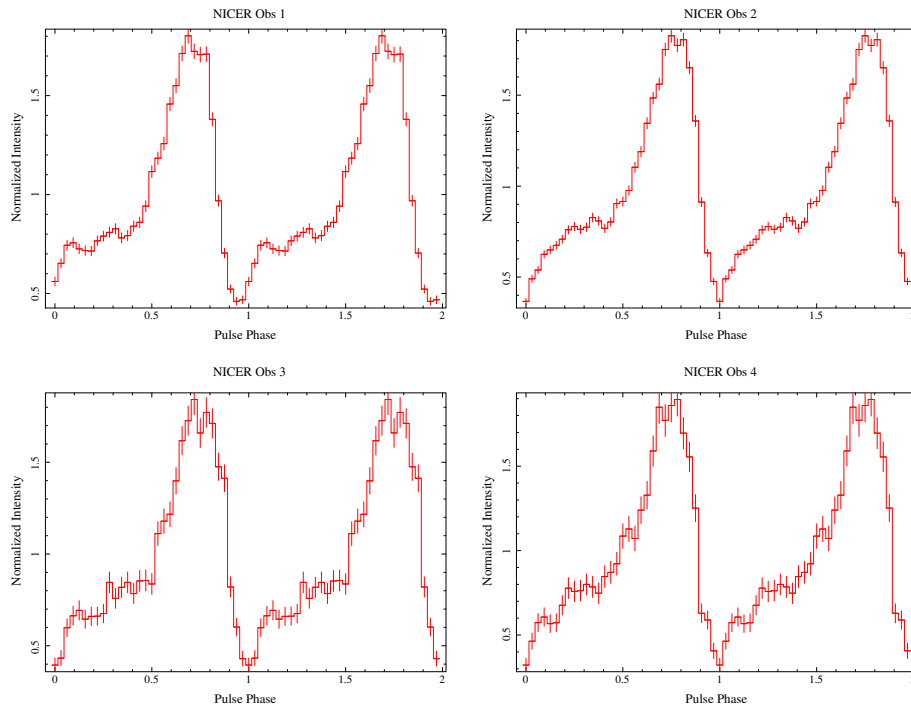
Appendix. Pulse profile evolution from NICER observations

Figure 8 shows the pulse profiles of 2S 1553–542 during different NICER observations.

Figure 8. Pulse profiles of 2S 15553–542 for different NICER observations during the outburst. The top left shows the pulse profile for NICER Obs 1, the top right is Obs 2, the bottom left shows the pulse profile for Obs 3 and the bottom right shows the pulse profile for Obs 4.

References

Apparao K. M., Bradt H. V., Dower R. G., *et al.* 1978, Nature, 271, 225

Basko M. M., Sunyaev R. A. 1976, MNRAS, 175, 395

Baykal A., Stark M. J., Swank J. H. 2002, ApJ, 569, 903

Becker P. A., Klochkov D., Schönherr G., *et al.* 2012, A&A, 544, A123

Bildsten L., Chakrabarty D., Chiu J., *et al.* 1997, ApJS, 113, 367

Blum S., Kraus U. 2000, ApJ, 529, 968

Burrows D. N., Hill J. E., Nousek J. A., *et al.* 2005, SSRv, 120, 165

Burnard D. J., Arons J., Klein R. I. 1991, ApJ, 367, 575

Camero-Arranz A., Finger M. H., Ikhsanov N. R., *et al.* 2009, ApJ, 708, 1500

Davidson K. 1973, Nature Phys. Sci., 246, 1

Doroshenko V., Santangelo A., Doroshenko R., *et al.* 2014, A&A, 561, A96

Epili P., Naik S., Jaisawal G. K., *et al.* 2017, MNRAS, 472, 3455

Finger M. H., Beklen E., Narayana Bhat P., *et al.* 2009, arXiv e-prints, 0912.3847

Finger M. H., Wilson R. B., 1996, A&AS, 120, 209

Finger M. H., Wilson R. B., Harmon B. A. 1996, ApJ, 459, 288

Gehrels N., Chincarini G., Giommi P., *et al.* 2004, ApJ, 611, 1005

Gendreau K. C., Arzoumanian Z., Adkins P. W., *et al.* 2016, SPIE, 9905, 99051H

Ghosh P., Lamb F. K. 1979a, ApJ, 232, 259

Ghosh P., Lamb F. K. 1979b, ApJ, 234, 296

Harrison F. A., Craig W. W., Christensen F. E., *et al.* 2013, ApJ, 770, 103

Harding A. K. 1994, AIPC, 308, 429

Jaisawal G. K., Naik S., Gupta S., *et al.* 2021, JApA, 42, 33

Kabiraj S., Paul B. 2020, MNRAS, 497, 1059

Kelley R. L., Rappaport S., Ayasli S. 1983, ApJ, 274, 765

Kraus U., Nollert H. P., Ruder H., *et al.* 1995, ApJ, 450, 763

Krimm H. A. *et al.* 2013, ApJS, 209, 114

Leahy D. A. 1987, A&A, 180, 275

Lutovinov A. A., Tsygankov S. S. 2009, AstL, 35, 433

Lutovinov A. A., Buckley D. A. H., Townsend L. J., *et al.* 2016, MNRAS, 462, 3823

Mandal M., Pal S. 2022, MNRAS, 511, 1121

Mandal M., Pal S., Hazra M. 2021, The Astronomer's Telegram, 14308, 1

Mandal M., Pal S. 2022, Astrophysics and Space Science, 367, 112

Malacaria C., Bhargava Y., Coley J. B., *et al.* 2022, ApJ, 927, 194

Matsuoka M., Kawasaki K., Ueno S., *et al.* 2009, PASJ, 61, 999

Meegan C., Lichti G., Bhat P. N., *et al.* 2009, ApJ, 702, 791

Mushtukov A. A., Tsygankov S. S., Serber A. V., *et al.* 2015, MNRAS, 454, 2714

Müller D., Klochkov D., Caballero I., *et al.* 2013, A&A, 552, A81

Pahari M., Pal S. 2012, MNRAS, 423, 3352

Parmar A. N., White N. E., Stella L. 1989, ApJ, 338, 373

Raichur H., Paul B. 2010, MNRAS, 406, 2663

Reig P., Nespoli E. 2013, A&A, 551, A1

Remillard R. A., Loewenstein M., Steiner J. F., Prigozhin G. Y., *et al.* 2022, AJ, 163, 130

Reynolds A. P., Parmar A. N., Stollberg T. M., *et al.* 1996, A&A, 312, 872

Schönherr G., Wilms J., Kretschmar P., *et al.* 2007, A&A, 472, 353

Serim M. M., Özüdoğru Ö. C., Dönmez Ç. K., *et al.* 2022, MNRAS, 510, 1438

Sugizaki M., Mihara T., Nakajima M., *et al.* 2017, PASJ, 69, 100

Staubert R., Shakura N. I., Postnov K., *et al.* 2007, A&A, 465, L25

Tsygankov S. S., Lutovinov A. A., Krivonos R. A., *et al.* 2016, MNRAS, 457, 258